Chinese Chemical Letters 31 (2020) 1392–1397

Contents lists available at ScienceDirect

Chinese Chemical Letters

journal homepage: www.elsevier.com/locate/cclet

Communication

In-situ conversion of Ni_2P/rGO from heterogeneous self-assembled NiO/rGO precursor with boosted pseudocapacitive performance

Ge Song[a,b], Zonglin Yi[c], Lijing Xie[a], Zhihong Bi[a,b], Qian Li[d], Jingpeng Chen[a,b], Qingqiang Kong[a], Chengmeng Chen[a,e,*]

[a] *CAS Key Laboratory of Carbon Materials, Institute of Coal Chemistry, Chinese Academy of Sciences, Taiyuan 030001, China*
[b] *University of Chinese Academy of Sciences, Beijing 100049, China*
[c] *College of Materials Science and Engineering, Taiyuan University of Technology, Taiyuan 030024, China*
[d] *Department of Chemical Engineering, Waterloo Institute of Nanotechnology, University of Waterloo, Waterloo, Ontario N2L 3G1, Canada*
[e] *Center of Materials Science and Optoelectronics Engineering, University of Chinese Academy of Sciences, Beijing 100049, China*

ARTICLE INFO

Article history:
Received 4 February 2020
Received in revised form 1 March 2020
Accepted 17 March 2020
Available online 18 March 2020

Keywords:
2D heterostructure
Ni_2P/rGO
Electrochemical active
Supercapacitor
DFT

ABSTRACT

Two-dimensional (2D) heterostructural Ni_2P/rGO is successfully fabricated by *in-situ* phosphating self-assembled NiO/rGO composites and shows the enhanced electrochemical performances. In this design, the rGO sheets effectively reduce the lattice strain created during the phase transformation from NiO to Ni_2P, thereby maintaining ultrathin nanostructures of Ni_2P. The resulting Ni_2P/rGO layered heterostructure gives the composite plenty of pores or channels, good electrical conductivity and well-exposed active sites. Density functional theory (DFT) calculation further demonstrates that the Fermi energy level and electron localize of near Ni atoms in Ni_2P is higher than that of NiO, which endow Ni_2P with faster and more reversible redox reactivity in dynamic. Benefiting from their structural and compositional merits, the as-synthesized Ni_2P/rGO exhibits high specific discharge capacity and excellent rate performance. Furthermore, a hybrid supercapacitor built with Ni_2P/rGO and activated carbon shows a high specific energy of 38.6 Wh/kg at specific power of 375 W/kg.

The discovery of graphene in 2004 motivated great interests in research on two-dimensional (2D) layered materials, such as hexagonal boron nitride, black phosphorus and layered double hydroxides (LDH) [1]. Due to their compelling electronic properties, excellent mechanical strength and ultrahigh specific surface area, 2D layered materials have attracted extensive attentions in the fields of catalysis [2,3], energy storage [4] and sensing platforms. However, the easy-restacking drawback of 2D materials severely restricts its practical application [5,6]. To solve the problem, the construction of heterostructures is regarded as an efficient strategy to suppress agglomeration and combine the advantages of different components [2,7,8].

This paper mainly focuses on the application of 2D heterostructure in supercapacitors, especially the transition metal-based battery-type materials in hybrid supercapacitors [9–11]. Commonly, battery-type materials such as RuO_2, $Ni(OH)_2$, $Co(OH)_2$, NiO, Co_3O_4, hold the appearance of evident redox peaks in CV curves, significant plateaus in GCD profiles, and variable ratio of ΔQ to ΔV [9,12,13]. The design of 2D heterostructure, highly dispersed and orderly self-assembly of two components at the nanometer scale, is favorable for controlling abundant porosity and taking advantages of different components [14–16]. For example, 2D/2D heterostructural $NiMoO_4$/MXene has been synthesized *via* hydrothermal method and post-calcination. The ultrafast charge transfer and more accessible active centers have been provided in the heterostructure, indicating its potential application in supercapacitors [15]. In our previous work, we reported the more efficient electrochemical active in the designed 2D layered heterostructural NiO/rGO [16]. The developed pore structure caused by the alternated self-assembling of NiO and rGO nanosheet would promote the sufficient contact between electrolyte and electrode, leading to sufficient redox reactions, which therefore enhance the electrochemical characteristic of 2D layered NiO/rGO electrode in supercapacitor [14,17,18]. However, transition metal hydroxide/oxides show the slow electron transmission in dynamics and thus lead to poor power performances [19,20]. In terms of above problems, phosphating strategy is a resultful solution [21–24]. Density functional theory (DFT) computations of various transition metal phosphides have revealed the corporation of phosphorus atoms into the metal lattice endowing transition

---

[*] Corresponding author.
E-mail address: ccm@sxicc.ac.cn (C. Chen).

https://doi.org/10.1016/j.cclet.2020.03.046
1001-8417/

metal phosphides with metalloid characteristics [25,26] and superior electrical conductivity [27–29], which is highly desired for superior electrochemical performances. Generally, the gas-solid phase reaction based on the pyrolysis of hypophosphite has been widely used for the shape-controlled synthesis of transition metal phosphides [25,30]. However, ultrathin precursor nanosheets usually tend to aggregate or sinter owing to the lattice strains induced by phosphorus substitution during the phase transformation process [31]. Thus far, the design of stable and active Ni_2P/rGO heterostructure is still lacking.

Considering the above viewpoints, we demonstrate an electrode design strategy in attempt to make Ni_2P uniformly disperse on rGO nanosheets to obtain 2D heterostructure Ni_2P/rGO composites. The obtained 2D heterostructural Ni_2P/rGO possesses several advantages: (1) the large electrochemical active sites of Ni_2P can be maintained in the heterostructure as the restacking of Ni_2P nanosheets is effectively inhibited; (2) the insertion of rGO can provide rapid electron transport between the graphene layers and Ni_2P nanosheets; (3) two types of nanosheets as building blocks could lead to plenty of pores or channels during the preparation of 2D heterostructural Ni_2P/rGO, which can effectively shorten the ion/mass transport distance. Furthermore, according to DFT calculations, the electronic structure and reactivity of Ni_2P/rGO can be greatly improved by phosphorus substitution. With large electrochemical active sites, abundant porosity and high electrical conductivity, 2D heterostructural Ni_2P/rGO can be a promising candidate towards advanced supercapacitor.

The synthesizing process of the Ni_2P/rGO is illustrated in Fig. 1. First, $Ni(OH)_2$/GO was prepared by our previous methods [16]. Through the anneal process, $Ni(OH)_2$/GO transformed into NiO/rGO [3]. SEM images of NiO/rGO in Figs. 2a and b show the layer-by-layer 2D structure, and the hexagonal NiO uniformly disperse on rGO nanosheets (Fig. 2c). After phosphating, the 2D layered structure is well inherited in Ni_2P/rGO (Figs. 2e and f), indicating the stability of 2D heterostructure, which is very important for the electrode in supercapacitor. The alternated stacking of the two assembled units effectively prevents the respective agglomeration and exposes active sites. Meanwhile, the 2D heterostructure renders the Ni_2P/rGO composite with large specific surface area (about 86 m^2/g shown in Table S1 in Supporting information) and appropriate pore-size distribution (Fig. S5 in Supporting information), which facilitate electrolyte ions penetration and accommodate volume expansion during electrochemical processes [32,33]. More importantly, Ni_2P well distributed on rGO sheets show smaller lateral size compared to that of NiO precursor, which is beneficial to the exposure of active sites and the promotion of redox activity [29]. As shown in Figs. S6d-f (Supporting information), compared with Ni_2P/rGO, pure Ni_2P shows agglomerated structure which is not favorable for effective contact between the active material and electrolyte, leading to worse electrochemical performance.

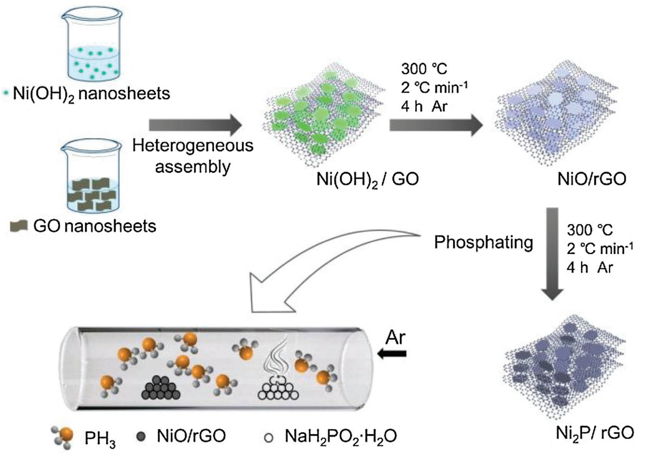

Fig. 1. Schematic illustration for the fabrication process of Ni_2P/rGO composite.

The purity and crystalline phase of $Ni(OH)_2$/GO, NiO/GO and Ni_2P/rGO were characterized by XRD in Fig. 3a. All XRD peaks of $Ni(OH)_2$/GO precursor was indexed to α-phase $Ni(OH)_2{\cdot}0.75H_2O$ (JCPDS No. 38-0715) [19]. After low temperature treatment, three new peaks appear and are indexed to NiO (JCPDS No. 44-1159) [18], revealing that pure and single-phase NiO was prepared. And the (012) crystal planes with inter-planar spacing of 0.208 nm can be observed in Fig. 2d. After further phosphorization, three peaks of NiO disappear, while some new peaks emerge, which matched well with the diffractions of (111), (201), (210), (300), (400) and (321) crystalline planes of Ni_2P (JCPDS No. 03-0953) [25,27,34,35], indicating a complete conversion of NiO to Ni_2P. The XRD data of pure NiO and Ni_2P are provide in Fig. S4 (Supporting information), demonstrating the full conversion form NiO/rGO to Ni_2P/rGO. It is interesting that the (201) and (111) crystalline planes of single crystal Ni_2P can be observed, corresponding to the inter-planar spacings of 0.202 and 0.224 nm in Fig. 2h, which further supports the XRD results [19,28,34,36]. Furthermore, there is no diffraction peaks observed for rGO nanosheets in three samples, which can be ascribed to the effective inhibition of rGO aggregation in 2D Ni_2P/rGO heterostructure [37].

The surface electronic states and chemical compositions of NiO to Ni_2P were further studied by X-ray photoelectron spectroscopy (XPS). Compared with the spectrum of NiO/rGO in Fig. 3b, two new peaks around 135 eV and 190 eV can be found in the spectrum of Ni_2P/rGO, indicating successful incorporation of P elemental after phosphating process. As shown in Fig. 3c, 855.7, 853.8 (Ni $2p_{3/2}$) and 872.5 (Ni $2p_{1/2}$) eV are the characteristic peaks of Ni^{2+} in NiO/rGO [11], while the peaks centered at 853.5, 870.5 eV in Fig. 3c and 129.9 eV in Fig. 3d are assigned to $Ni^{\delta+}$ and $P^{\delta-}$ in Ni_2P [30,36], meaning the conversion of NiO to Ni_2P, which support the results of XRD. What is more, the peak value of $Ni^{\delta+}$ (853.5 eV) is slightly higher than that of metal Ni (852.6 eV), corroborating the presence of slightly positive charge $Ni^{\delta+}$ (δ is likely close to 0) [38,39]. Similarly, the P 2p binding energy value (129.9 eV) is slightly less than that of elemental P (130.0 eV), indicating the P species has a small negative charge value ($P^{\delta-}$) [40]. The weaker electron restraint endow Ni_2P with a metalloid characteristic and show higher conductivity [41], which is further proved by Bader charge method [42]. Initially, crystallographic planes were optimized according to the crystal structure of Ni_2P and NiO in Fig. S5. The corresponding top view and side view are shown in Fig. 4a, including (111), (201) for Ni_2P and (012), (101) for NiO. As shown in Table S2 (Supporting information), the Bader charge results show that Ni atoms in Ni_2P surfaces possessed approximately 1|e| charge less than those in NiO surfaces. This indicates that Ni atoms on the Ni_2P surface have fewer electrons bound by anions, meaning Ni_2P with metalloid characteristics, which is consistent with the XPS results. Moreover, more free electrons around Ni atom can further improve the electrochemical performance, and that would be proved in the next part. In addition, the peaks at 856.6 (Ni $2p_{3/2}$) and 874.6 eV (Ni $2p_{1/2}$) corresponding to Ni^{2+} in Fig. 3c and the typical peak at 134.9 eV of phosphate species [23] in Fig. 3d are most likely in the form of phosphate salts as a consequence of superficial passivation [31]. Besides, phosphate ions are also generated through excess PH_3 further reacting with H_2O and then adhere to the surface of Ni_2P/rGO during the phosphating reaction.

The electrochemical properties of Ni_2P, NiO/rGO and Ni_2P/rGO are studied through cyclic voltammetry (CV) and galvanostatic charging/discharging (GCD) tests in three-electrode cell. Fig. 5a shows the CV curves of Ni_2P, NiO/rGO and Ni_2P/rGO from 0 to 0.6 V

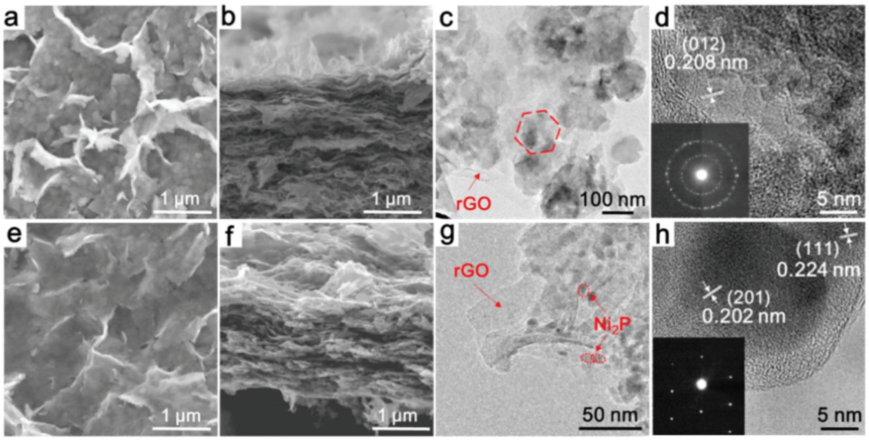

Fig. 2. SEM image (a,b) and TEM image (c,d) of NiO/rGO. SEM image (e,f) and TEM image (g,h) of Ni_2P /rGO. The inset of (d) and (h) show the corresponding SAED pattern of NiO/rGO and Ni_2P/rGO, respectively.

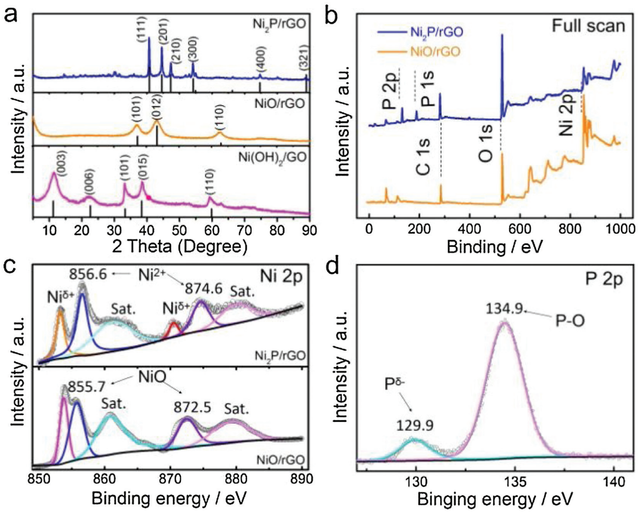

Fig. 3. (a) XRD patterns of $Ni(OH)_2$/GO, NiO/rGO and Ni_2P/rGO. (b) XPS full spectra and (c) Ni 2p spectra of Ni_2P/rGO and NiO/rGO. (d) P 2p spectra of Ni_2P/rGO.

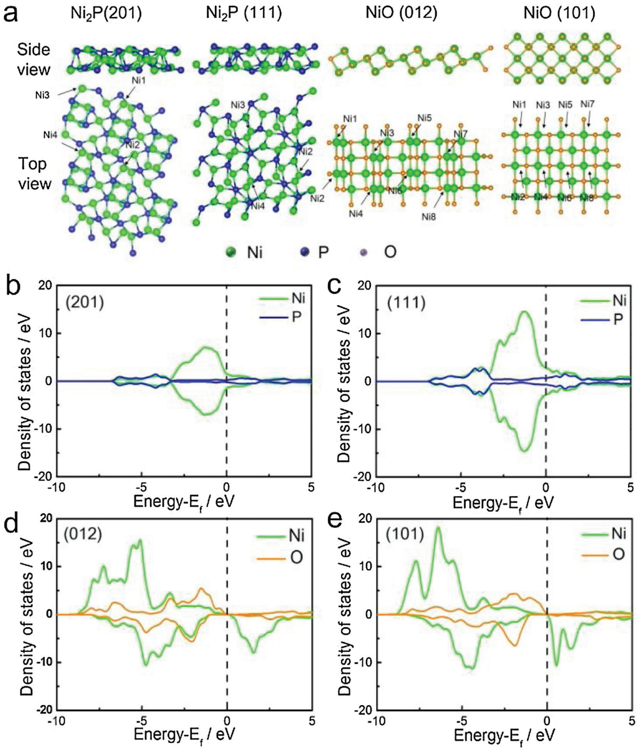

Fig. 4. (a) Top and side views for optimized structure of Ni_2P (201), Ni_2P (111), NiO (012), NiO (101) planes. Three-dimensional model was displayed by VESTA [43]. PDOS of (b) Ni_2P (201), (c) Ni_2P (111), (d) NiO (012), (e) NiO (101) surfaces.

at 10 mV/s. Obviously, three curves all display one pair of distinct redox peaks, indicating rapid reversible redox reactions on the surface of the battery-type materials [44,45]. The reaction mechanism of Ni_2P is similar with NiO described in the following [30]:

$$NiO + OH^- \leftrightarrow NiOOH + e^- \quad (1)$$

$$Ni_2P + 2OH^- \leftrightarrow Ni_2P(OH)_2 + 2e^- \quad (2)$$

Generally, the integrated area of the CV curve can give a more intuitive indication of the capacity [6]. Compared with NiO/rGO and pure Ni_2P, a larger integral area of the CV curve (Fig. 5a) and longer discharge time (Fig. 5b) can be seen for Ni_2P/rGO electrode, illustrating the improved specific discharge capacity. The CV curves of Ni_2P/rGO at various scan rates show little change and polarization as shown in Fig. 5c, indicating the good rate capability of Ni_2P/rGO. According to GCD curves of Ni_2P/rGO (Fig. 5d), NiO/rGO (Fig. S8 in Supporting information) and pure Ni_2P (Fig. S9 in Supporting information), the specific discharge capacities at diverse specific current were shown in Fig. 5e. Furthermore, the electrochemical properties of both the pure rGO and $Ni(OH)_2$ were tested in Figs. S10 and S11 (Supporting information). By contrast, pure Ni_2P show less specific capacity than Ni_2P/rGO, due to inadequate exposure of the active site resulting from the severe agglomeration, which is consistent with our analysis in SEM. To further illustrate the enhanced electrochemical performance of Ni_2P/rGO compared to NiO/rGO, we made an in-depth analysis of Ni_2P and NiO. The reactivity of materials is determined by the chemical bonds on the metal sites and the corresponding electronic environment [29]. The chemical bonds were discussed in depth firstly. The length of the Ni-P bond (2.199 Å) is longer than Ni-O (2.054 Å), according to the crystal structures of Ni_2P and NiO in Fig. S7 (Supporting information). And the Pauling electronegativity of P is 2.19, which is weaker than element O of 3.44. Based on

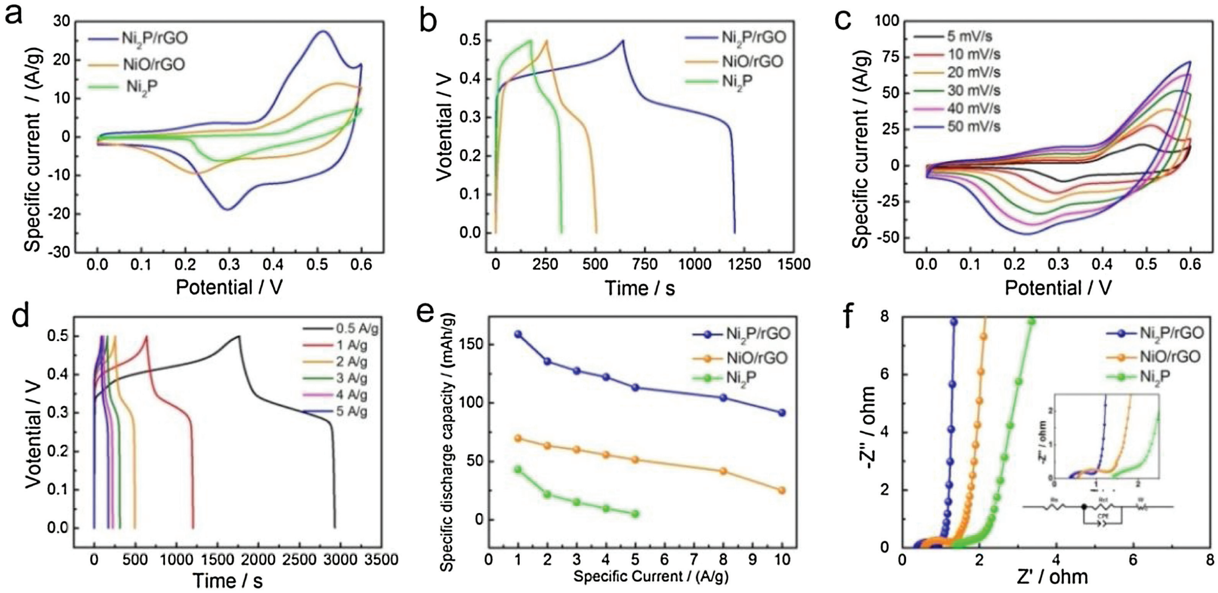

Fig. 5. (a) CV curves of Ni_2P/rGO, NiO/rGO and Ni_2P at a scanning rate of 10 mV/s in 6 mol/L KOH solution. (b) The galvanostatic charge /discharge curves of Ni_2P/rGO, NiO/rGO and Ni_2P at the specific current of 1 A/g. (c) CV curves of Ni_2P/rGO at different scan rates. (d) The GCD curves of Ni_2P/rGO at different specific currents. (e) Specific discharge capacities of Ni_2P/rGO, NiO/rGO and Ni_2P electrodes at different specific currents. (f) Nyquist plots of Ni_2P/rGO, NiO/rGO and Ni_2P electrodes in the frequency range of 100 kHz to 0.01 Hz. The inset shows the enlarged EIS of the electrodes.

the electronegativity value, the characteristics of the chemical bond can be evaluated by the following equation [46]:

$$\text{Covalent character } (\%) = 100 \times \exp\left[-0.25\,(X_a - X_b)^2\right] \quad (3)$$

where X_a and X_b represent the electronegativity values of anions and cations, respectively. The high degree of covalence suggests a high degree of sharing electrons in the chemical bonds [29]. The covalent characteristics of Ni-P and Ni-O were calculated to be 98.06% and 55.70%, respectively. This is to say, the longer bond (Ni-P) and the smaller electronegativity (P) reduce electron transfer from Ni to anion and increase the ratio of sharing electrons, leading to more electrons in Ni of Ni-P. Thus less energy is required to extract or obtain electrons in the redox reaction, resulting in enhanced electrode dynamics of Ni_2P. Furthermore, the electronic environment around metal sites was discussed by calculating projected density of states (PDOS). Fermi energy level was set to zero in all diagrams. Generally, it is the electrons in 3d orbitals that participate in chemical reactions for transition metals. Density of states of Ni in Ni_2P is enhanced near the Fermi energy level and higher electron localize near Ni atoms in Ni_2P surfaces, which decreases the migration energy of electrons in electrochemical reaction. Therefore, the introduction of P can improve the kinetics during the electrochemical processes, which is in favor of the specific capacities. Based on the above discussion, theoretical calculations was used to prove that Ni_2P has higher electrical conductivity and chemical reactivity than NiO, meanwhile, the decreased size of Ni_2P nanosheets enables the effective use of reactive sites. Therefore, the electrochemical performance of Ni_2P/rGO is significantly better than NiO/rGO. What's more, the introduction of rGO hinders the agglomeration of Ni_2P and improves the conductivity effectively, verifying the superior storage properties of Ni_2P/rGO compared to pure Ni_2P. A comparison of the electrochemical properties of the Ni_2P/rGO with recently reported materials is shown in Table S2. It can be revealed that the specific capacitance of the Ni_2P/rGO with 2D heterostructural in this work is superior to that of the recent reports.

Furthermore, electrochemical impedance spectroscopy (EIS) measurements were carried out to study the ion and electron transport kinetics in the Ni_2P/rGO, NiO/rGO and pure Ni_2P electrodes. As shown in Fig. 5f, three Nyquist plots contain one semicircle and a linear segment in the high and low frequency region, respectively. The intercept of semicircle on the real axis represent equivalent series resistance (R_S), which consists of the resistance of the electrode material and the ionic resistance of the electrolyte [26]. The diameter of the semicircle represents the charge transfer resistor (R_{ct}) of the electrode/electrolyte interface in a Faraday reaction. Ni_2P contribute with better electrical conductivity compared to NiO and rGO can constitute a conductive network to improve conductivity effectively. Thus Ni_2P/rGO has the ability of faster charge transfer within the electrode and at the electrode/electrolyte interface [28]. Table S3 (Supporting information) shows the results for EIS circuit simulation by equivalent circuit fitting (inset of Fig. 5f). The straight line portion of the low frequency region indicates the electrolyte diffusion impedance. In Fig. 5f, Ni_2P/rGO has a more vertical line than those of other electrodes, suggesting that Ni_2P/rGO with 2D layered structure greatly shortens the ion diffusion path, which helps ions quickly transport to the surface of Ni_2P nanosheet for electrochemical reaction.

In order to further evaluate the practical application of Ni_2P/rGO electrode, a hybrid supercapacitor encapsulated in button cell was fabricated using Ni_2P/rGO as the cathode and active carbon (AC) as the anode in 6 mol/L KOH. Fig. 6a shows the CV curves of Ni_2P/rGO and AC electrodes at a scan rate of 10 mV/s. A series of CV curves of hybrid supercapacitor at different voltage windows are shown in Fig. 6b. The operating voltage can be steadily extended to 1.6 V while severe polarization reaction occurs near 1.7 V. Furthermore, as the scan rate increases from 5 mV/s to 100 mV/s, the CV curve exhibits a non-rectangular shape with redox peaks at 0–1.6 V (Fig. 6c), indicating that the capacity is mainly from the redox reaction. At the same time, the similar shape of all CV curves means good rate performance for Ni_2P/rGO//AC hybrid supercapacitor. The specific discharge capacity calculated from the GCD curves in Fig. 6d was based on the total mass of the active materials in two

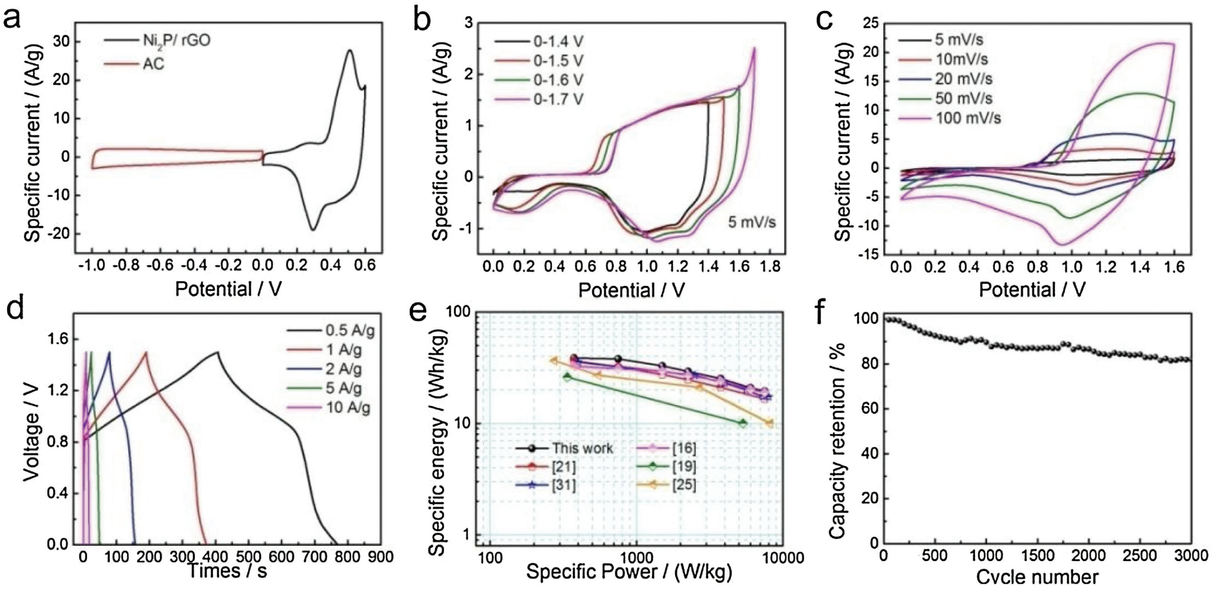

Fig. 6. Electrochemical performances of the Ni_2P/rGO // AC ASC device: (a) CV curves of Ni_2P/rGO and AC electrodes at a scan rate of 10 mV/s in 6 mol/L KOH electrolyte. (b) CV curves of the ASC devices at 5 mV/s with different cell voltage. (c) CV curves of the HSC devices collected at different scan rates. (d) GCD curves of HSC devices obtained at different specific currents. (e) Ragone plots of as-assembled Ni_2P/rGO//AC HSC against previous reports. (f) Cycling performance of the HSC device at a specific current of 5 A/g.

electrodes. Similarly, the GCD curve is not a straight line, which is consistent with the results of the CV curve analysis. According to Eqs. S6 and S7 in Supporting information, the hybrid supercapacitor specific energy reaches 38.6 Wh/kg at a power density of 375 W/kg. Even at a specific power of 7500 W/kg, it still delivers 19.5 Wh/kg, which is higher than NiO/rGO//AC in our previous work [16]. What is more, the specific power and energy of Ni_2P/rGO//AC hybrid supercapacitor are superior to, or at least similar to, that of other reported hybrid supercapacitor as shown in Fig. 6e, such as NiCoP//AC (16.65 Wh/kg at 7500 W/kg) [21], Fe_2O_3//Ni_2P (35.5 Wh/kg at 400 W/kg) [31], Ni_2P/NF//AC (10 Wh/kg at 5332 W/kg) [19] and Ni_2P//AC (36.5 Wh/kg at 275 W/kg) [25]. In Fig. 6f, the hybrid supercapacitor device also shows the good electrochemical stability, with 82% of the device capacitance retained even after 3000 charging and discharging.

In summary, we successfully designed and fabricated battery-type Ni_2P/rGO nanocomposite with 2D layered heterostructure by pre-thermal treatment of self-assembling $Ni(OH)_2$/GO precursor and post-low temperature phosphating. The 2D layered structure with opened porosity provides the facile channel for both ion diffusion and electron transfer. In this composite, rGO act as the 2D interlayer spacer to prevent the aggregation and as the conductive network for efficient electron transport, while smaller size of Ni_2P nanosheets have been identified through TEM observation to facilitates full use of active sites. Furthermore, the DFT-based calculation reveals that Ni_2P improve charge transfer and accelerate the kinetics of Faraday reaction, thus significantly enhance electrochemical performance. By virtues of the unique structure and composition, the Ni_2P/rGO nanocomposite exhibits high specific discharge capacity (158.9 mAh/g at 1 A/g, 113.2 mAh/g at 5 A/g). More importantly, the hybrid supercapacitor Ni_2P/rGO//AC displays a specific energy of 38.6 Wh/kg^{-1} at a specific power of 375 W/kg. This work provides new insights into the design of advanced electrode materials with 2D heterostructure for hybrid supercapacitors.

Declaration of competing interest

The authors declare that they have no known competing financial interests or personal relationships that could have appeared to influence the work reported in this paper.

Acknowledgments

This research was supported by the DNL Cooperation Fund, CAS (No. DNL201915), National Science Foundation for Excellent Young Scholars of China (No. 21922815), National Natural Science Foundation of China (No. 21975275) and Key Research and Development (R&D) Projects of Shanxi Province (No. 201903D121007).

Appendix A. Supplementary data

Supplementary material related to this article can be found, in the online version, at doi:https://doi.org/10.1016/j.cclet.2020.03.046.

References

[1] C.L. Tan, X.H. Cao, X.J. Wu, et al., Chem. Rev. 117 (2017) 6225–6331.
[2] Y.X. X, B. Li, S.S. Zheng, J. Mater. Chem. A 6 (2018) 22070–22076.
[3] S.S. Zheng, X.T. Guo, H.G. Xue, Chem. Commun. 55 (2019) 10904–10907.
[4] G. Gao, H.B. Wu, X.W. Lou, Adv. Energy Mater. 4 (2014) 1400422.
[5] P. Das, Q. Fu, X. Bao, Z.S. Wu, J. Mater. Chem. A 6 (2018) 21747–21784.
[6] X.W. Dong, Y.D. Zhang, B. Ding, et al., J. Power Sources 390 (2018) 208–214.
[7] S.S. Shi, Z.P. Li, Y. Sun, et al., Nano Energy 48 (2018) 510–517.
[8] Z.S. Wu, G.M. Zhou, L.C. Yin, et al., Nano Energy 1 (2012) 107–131.
[9] M. Zhou, H. Zhao, F. Ko, et al., J. Power Sources 440 (2019) 227146.
[10] Y. Yang, Y. Zhou, Z. Hu, et al., J. Alloys Compd. 772 (2019) 683–692.
[11] P. Wang, H. Zhou, C. Meng, et al., Chem. Eng. J. 369 (2019) 57–63.
[12] N. Zhao, H. Fan, J. Ma, et al., J. Power Sources 439 (2019) 227097.
[13] T. Brousse, D. Belanger, J.W. Long, J. Electrochem. Soc. 162 (2015) A5185–A5189.
[14] L. Peng, X. Peng, B. Liu, et al., Nano Lett. 13 (2013) 2151–2157.
[15] Y. Wang, J. Sun, X. Qian, et al., J. Power Sources 414 (2019) 540–546.
[16] Q. Li, Q. Wei, L.J. Xie, et al., RSC Adv. 6 (2016) 46548–46557.
[17] Y. Shao, M.F. El-Kady, J. Sun, et al., Chem. Rev. 118 (2018) 9233–9280.
[18] D. Li, Y. Gong, M. Wang, C. Pan, Nano-Micro Lett. 9 (2017) 16.
[19] K. Zhou, W. Zhou, L. Yang, et al., Adv. Funct. Mater. 25 (2015) 7530–7538.
[20] T. Zhai, L. Wan, S. Sun, et al., Adv. Mater. 29 (2017) 1604167.
[21] X.M. Zhang, A.P. Wu, X.W. Wang, et al., J. Mater. Chem. A 6 (2018) 17905–17914.
[22] R. Wu, B. Xiao, Q. Gao, et al., Angew. Chem. Int. Ed. 57 (2018) 15445–15449.
[23] Y. Wang, C. Wu, Z. Wu, et al., Chem. Commun. 54 (2018) 9341–9344.
[24] J. Wang, R. Zhang, Y. Liu, et al., Chem. Commun. 54 (2018) 7195–7198.
[25] Y. Jin, C. Zhao, Q. Jiang, C. Ji, Appl. Surf. Sci. 450 (2018) 170–179.
[26] Y. Lan, H. Zhao, Y. Zong, et al., Nanoscale 10 (2018) 11775–11781.
[27] Z. Lv, Q. Zhong, Y. Bu, Appl. Surf. Sci. 439 (2018) 413–419.
[28] T. Liu, A. Li, C. Wang, et al., Adv. Mater. 30 (2018) 1803590.
[29] J. Li, Z. Liu, Q. Zhang, et al., Nano Energy 57 (2019) 22–33.

[30] S. Liu, K.V. Sankar, A. Kundu, et al., ACS Appl. Mater. Interfaces 9 (2017) 21829–21838.
[31] D. Wang, L.B. Kong, M.C. Liu, Y.C. Luo, L. Kang, Chem. -Eur. J. 21 (2015) 17897–17903.
[32] X.R. Li, J.L. Wei, Q. Li, et al., Adv. Funct. Mater. 28 (2018) 1800886.
[33] G.Q. Yuan, S.K. Yu, J. Jie, et al., Chin. Chem. Lett. (2019), doi:http://dx.doi.org/10.1016/j.cclet.2019.12.034.
[34] Y. Jin, C. Zhao, L. Wang, et al., Int. J. Hydrogen Energy 43 (2018) 3697–3704.
[35] X. Dai, H. Song, Z. Yan, et al., New J. Chem. 42 (2018) 19917–19923.
[36] H. Li, X. Wang, Z. Zhao, et al., ChemElectroChem 6 (2019) 404–412.
[37] D.Y. Cai, M. Song, J. Mater. Chem. 17 (2007) 3678–3680.
[38] Z. Sun, M. Zhu, X. Lv, et al., Appl. Catal. B 246 (2019) 330–336.
[39] W. Tang, J. Wang, L. Guo, et al., ACS Appl. Mater. Interfaces 9 (2017) 41347–41353.
[40] R.Q. Zhou, J.F. Zhang, Z.L. Chen, et al., Electrochim. Acta 258 (2017) 866–875.
[41] S. Li, M. Hua, Y. Yang, et al., J. Mater. Chem. A 7 (2019) 17386–17399.
[42] M. Yu, D.R. Trinkle, J. Chem. Phys. 134 (2011) 064111.
[43] K. Momma, F. Izumi, J. Appl. Crystallogr. 44 (2011) 1272–1276.
[44] Z. Shi, L. Xing, Y. Liu, Y. Gao, J. Liu, Carbon 129 (2018) 819–825.
[45] P. Wu, S. Cheng, M.H. Yao, et al., Adv. Funct. Mater. 27 (2017) 1702160.
[46] C. Liu, C. Zhang, H. Fu, X. Nan, G. Cao, Adv. Energy Mater. 7 (2017) 1601127.